American Society of Mechanical Engineers

ASME Accepted Manuscript Repository

Institutional Repository Cover Sheet

Scale Effects on Performance of BLDC Micromotors for Internal Biomedical Applications: a Finite Element Analysis

Gabriel Villalba-Alumbreros[1], Carlos Moron-Alguacil[1], Miguel Fernandez-Munoz[1], Ignacio Valiente-Blanco[1], Efren Diez-Jimenez[1*]

[1] Mechanical Engineering Area, Universidad de Alcalá, Ctra. Madrid-Barcelona, Km 33,600, Alcalá de Henares, 28805, Spain

* Corresponding author: efren.diez@uah.es

Abstract: Micromotors can be used to build up complex microtools for internal medical applications as for example steerable catheters or optical and ultrasonic imaging system. The thinner and smaller the micromotors are, the less invasive is the implantation. However, miniaturization of motors implies some limitations in torque, speed and efficiency. This paper theoretically analyses the scale effects on torque, efficiency and thermal behaviour of high torque permanent magnet BLDC motors with ferromagnetic core coils operating in different in-body environment. Using a finite element model of a 2-phase BLDC motor, scalability laws are provided for diameters between 0.1 and 100 mm and current densities between 1 and 1000 A/mm^2. Based in the impact of the cogging torque and overheating of the motor, scale dependent operational limits are calculated. Operational threshold can be determined at the point where cogging torque becomes dominating over total torque, limiting the use of traditional iron-core motors in the microscale. Current density limits are provided based on three representative in-body thermal scenarios: respiratory tract, body fluid and blood torrent. Maximum current densities and corresponding torque and efficiency have been obtained for different micromotor sizes considering safe in-body temperature operation as threshold. It is demonstrated that micromotors of sizes down to 0.1 mm diameter could be used in internal body environments with acceptable performance.

Keywords— BLDC motor, micromotor, electromagnetic micromotor, scale effect, thermal behavior, minimally invasive tools, internal medical devices, high torque biomedical actuators

1   Introduction

Miniaturization of motors and actuation systems potentially opens new frontiers in optical measurement tools [1], electronics for data storage [2], optical positioning systems [3], robots for small cavities exploration [4], manipulators for manufacturing and assembly of micro-actuators and transducers [5]. Of especial interest, micromotors and rotary actuators systems can be used to

build up complex microtools for internal medical applications as for example in optical gastroscopy [6], colonoscopies [7], intravascular imaging [8], laparoscopic surgery [9] or localized drug delivery [10].

If small and thin high torque micromotor are developed, a new generation of internal medical microtools could be developed for minimally invasive surgery and diagnostics. Micromotors connected in catheters end tips has been already proposed for use in optical and ultrasonic imaging [11]. Other potential example of application is a multiaxis steerable catheter including a set of high torque micromotors could be useful to go through intricate vessels paths. Another example, gimbal laser pointers having two or three micromotors could increase precision in ablation procedures. A final example is multiaxis microrobotic tweezers could reduce size of surgery and arthroscopies tools. Multiaxis anthropomorphic robotic arms are for surgery intervention have been widely used in paste decades and optimized using neural and deep learning techniques [12] [13]. Now we proposed to miniaturize those type of anthropomorphic robotic arms for minimally invasive surgery techniques. For all these new tools, high torque thin electromagnetic micromotors are critical components that require specific development.

These new tools will require high torque actuation systems to provide strong grabbing and moving capacity. Regularly, actuators include a gearhead that multiplies the torque [14,15], but for micromotors is much more difficult to implement due to increase complexity and number of parts [16],[17]. Whereas rotary motors in the macro-scale for sizes above 10 mm are clearly dominated by radial iron-core electromagnetic motors, these type of actuation systems are scant in the micro-scale. On the contrary, technologies used to build micromotors and actuators with diameters below 10 mm mainly include: electrostatic motors, piezo-electric actuators and low torque electromagnetic motors with no ferromagnetic cores, therefore it can be worth to explore the potential of high torque micromotors with ferromagnetic cores for internal medical devices. The main objective of the work hereby presented is to theoretically study and determine which would be the operational limits and the expected performance of miniaturized high torque electromagnetic micromotors inside human body environment as a function of the motor size.

Exploring high torque density micromotors for biomedical applications is one of the main objectives of H2020 UWIPOM2 project [18]. This project seeks to develop a micrometric-size high torque micromotor wirelessly powered [19]. The dimension targeted for this high torque micromotor is diameter smaller than 3 Frenches, i.e. diameter smaller than 1 mm and total lengths not larger than diameter. The present article has been prepared within the frame of this H2020 project.

Electromagnetic micromotors are typically divided in two categories: induction and permanent magnet micromotors. Induction micromotors are mainly composed of a set of windings that generate induction eddy currents in an electrically conductive rotor [20],[21], [22]. This type can also generate eddy currents and cogging torque if there are ferromagnetic cores in the stator [23], [24]. Operation of micromotors have been demonstrated in a typical size range from 1 to 10 mm, being the smallest electromagnetic motor 0.5 mm in size [25] of induction type, with a reduced torque capacity.

It is significant that no permanent magnet electromagnetic BLDC micromotors, smaller than 1 mm diameter, with ferromagnetic

core coils have been found in the literature. The use of core-less coils certainly limits the torque capacity of an electromagnetic motor and reduces the range of applicability of the technology in the micro-scale [24]. As we will demonstrate in this paper, cogging torque in the micro-scale plays a major role in this fact. Magnetic damping is a significant limitation in micromotors and electromagnetic devices [26–28].

Table 1 summarizes the main performance parameters of some electromagnetic motors found in the literature with sizes from 1 [11] to 10 mm [29].

Table 1 Electromagnetic motor characteristics

Motor Type	Diameter range evaluated [mm]	Torque density range [kNm/m^3]	km range [$\mu Nm/A$]	km density range [$\mu Nm/(m^3 \cdot A)$]
PM axial	1-10	$3 \cdot 10^{-4} - 3 \cdot 10^{0}$	$2 \cdot 10^{0} - 3 \cdot 10^{2}$	$1 \cdot 10^{0} - 7 \cdot 10^{1}$
PM radial	0.95-6	$6 \cdot 10^{-4} - 1 \cdot 10^{0}$	$4 \cdot 10^{-1} - 5 \cdot 10^{2}$	$2 \cdot 10^{-1} - 2 \cdot 10^{0}$
Ind. axial	4-10	$3 \cdot 10^{-2} - 3 \cdot 10^{-1}$	$2 \cdot 10^{-1} - 5 \cdot 10^{0}$	$5 \cdot 10^{-3} - 4 \cdot 10^{-2}$
Ind. radial	1.4-10	$2 \cdot 10^{-2} - 1 \cdot 10^{-1}$	$1 \cdot 10^{-2} - 7 \cdot 10^{2}$	$5 \cdot 10^{-2} - 1 \cdot 10^{0}$

Just a few studies have been focused on the dependency of the performance of electromagnetic motors with their characteristic length (L) or diameter. In most cases, the very basic motor figures of performance are presented as an exponential function of the characteristic length. Binns and Shimmin proposed a relationship between torque and magnet volume. In addition, they analytically evaluated the thermal aspects of the motor for different scales [30]. Assuming a constant current density, a perfect heat evacuation and linear behavior of the magnetic materials, the torque produced by the motor is proportional to L^4. As proposed by Kuang-Chen et al. in [31], when more realistic scenarios are considered, torque is proportional to L^3 and L^5 depending on the operational conditions. A deeper thermo-electrical study is carried out in [32] for general applications. A scalability law is there provided for the average heat transfer coefficient (h), which is proportional to between $h \propto L^{-1}$ and $h \propto L^{-0.5}$. Analysis of miniaturization effects are excellent tools to determine if the exploration of a technology is worth or not, in general, but even more critical for biomedical applications where additional requirements must be considered [33][34]. This type of analysis permits to save time and avoid mistakes and wrong trials before manufacturing real prototypes. Finite element analysis are key tools to perform scale analysis since they permit to accurately simulate physical behaviour of medical devices at any scale very rapidly [35].

In this work, we theoretically study which are the operational limits and the expected performance inside different human body environment as long as the motor is miniaturized. This permits to determine the maximum expected performance and torque values for different sizes of micromotors. The selected motor model is a 2 phases BLDC (Brushless DC) permanent magnet micromotor with ferromagnetic core windings. This design has been selected as a trade-off between high torque density potential and simplicity

of manufacturing of the parts and assembly. Stator is composed by laminations stock made in ferromagnetic material, wounded around with copper wires. Rotor is simply composed of a cylindrical permanent magnet diametrically magnetized. Bearings, whether rolling or plain, would be place at the top and bottom of the shaft. Bearings are not considered in the analysis.

Along this work, we theoretically determine the scalability effects on the main performance parameters of the micromotors. Scalability laws are obtained for torque, cogging torque and torque density of the motor. In addition, motor current constant, power losses, efficiency, heat generation and dissipation are also obtained and analyzed at scales between 100 mm and 0.1 mm. Current density limits are provided based on three representative in-body thermal scenarios: blood torrent, body fluid and respiratory tract. Maximum current densities and corresponding torque and efficiency have been obtained for different micromotor sizes considering safe in-body operation as threshold (Surface temperature of the motor lower than 43 ℃. This permits to determine the operational limits of these type of micromotors for a safe in-body operations. Specific examples and expected performance for different sizes of motors are given in final section.

2   Motor design and geometry description

A radial BLDC motor is proposed due to its wide applications and control simplicity. More specifically, the design is a 2-phase permanent magnet BLDC motor with ferromagnetic yokes, as shown in Fig. 1.
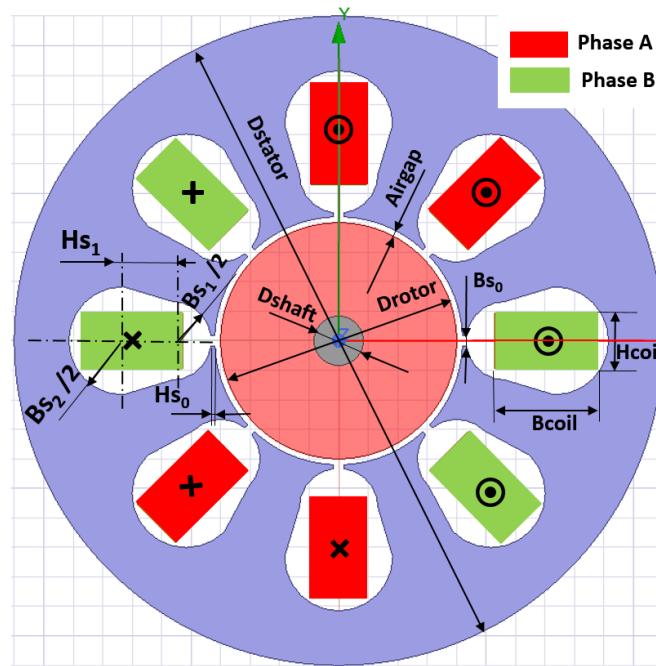

Fig. 1. Cross-section of the motor.

The rotor of the motor is mainly constituted by a single pole cylindrical permanent magnet mounted on a concentric ferromagnetic shaft. This configuration of the inner rotor is selected since manufacturing of multipolar permanent magnet rotors in the microscale is currently a limitation [36]. The permanent magnet material is $Nd_2Fe_{14}B$ grade N35 and it is diametrically magnetized with a remanence B_r = 1.23 T, a coercivity H_c = 890 kA/m and an electrical resistivity $\rho = 1.6 \cdot 10^{-6} \Omega \cdot m$. The rotor shaft is made of high-performant FeCo alloy Vacoflux 48 with a saturation polarization J_s = 2.3 T and a maximum relative magnetic permeability of $\mu_{max} = 18000$.

The stator of the motor is made by the stator armature and a 2-phase winding with a total of 4 coils, connected as shown in Fig. 1. The armature, made of Vacoflux 48 with the same properties as the rotor shaft material, is assembled as a laminated stack with lamination thicknesses independent of the motor size and equal to 0.35 mm in all cases. This lamination thickness can be easily found in the market and does not require from special micro-manufacturing techniques to be produced.

Each winding phase is composed by 4 slots. The coils in a single phase (A or B) are connected in series. Coils wire is made of high conductivity copper with a resistivity at 20ºC of $\rho_{293K} = 1.72 \cdot 10^{-8} \Omega \cdot m$ and a temperature sensitivity of $6.8 \cdot 10^{-11} \frac{\Omega \cdot m}{K}$. For all the explored sizes of the motors, ratio between the areas of the active coils and the area of the slot is about 50 %. Bulk coils (1 single turn) are considered for the shake of simplicity. This do not affect the calculations of resistive power losses in the windings since they are independent on the number of turns in our calculations.

In all the presented models, the length of the motor (L) is always considered equal to the stator outer diameter (D_{stator}). This is a good choice in order to keep a high compactness of the micromotor. Therefore, the *"characteristic length"* refers to the diameter and total length indistinctly.

Geometrical parameters are defined in Table 2 for a motor characteristic length $L = D_{stator}$ of 1 mm. Then, the motor geometry is volumetrically scaled proportionally to a scale factor between 0.1 and 100. Therefore, for all motor sizes, the aspect ratios remain constant.

Table 2 Values for 1 Milimeter Diameter Motor

Parameter	Value
Motor Diameter, D_{stator} [mm]	1
Motor Length, L [mm]	1
rotor-stator gap [mm]	0.01
Drotor [mm]	0.4
Dshaft [mm]	0.084
hcoil [mm]	0.093
Bs0 [mm]	0.017
Bs1 [mm]	0.134
Bs2 [mm]	0.184
Hs0 [mm]	0.007
Hs1 [mm]	0.059

3   Electromagnetic finite element model of the motor

The electromagnetic behaviour of the motor has been analysed by using a parametric 2D transient finite element model. The magnetic fields generated in the motor are calculated solving the 2D electromagnetic motion equation (1):

$$\nabla \times v\nabla \times A = J - \frac{1}{\rho}\left\{\frac{dA}{dt} + \nabla V\right\} + \nabla \times H_c \qquad (1)$$

Where A is the magnetic vector potential, v is the reluctivity,

J is the source current density, ρ is resistivity of the material,

$\frac{dA}{dt}$ is the total time derivative of the vector potential, V is the electrical potential, and H_c is the permanent magnet coercivity,

The 2D transient finite element model is solved using ANSYS Electronics 2019 R3 software. Similar models have been used for micro-magnetic gears analysis in [37,38]. In the transient model, rotor components are forced to spin concentrically with the stator and at a constant rotational speed. Motor performance figures are then obtained from post-processing of the magnetic field solution. As an example of such field, Fig. 2 shows the magnetic flux lines distribution inside a motor of 1 mm size at an arbitrary time step of the simulation.
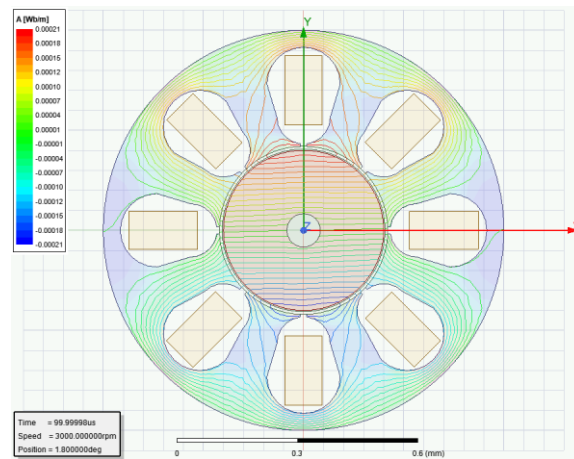
Fig. 2. Magnetic flux inside 1mm motor.

A sinusoidal current that flows into each winding phase is defined as:

$$I_{phase} = J \cdot A_c \cdot \sin(\omega_r \cdot t + \varphi) \qquad (2)$$

Where J is the current density, A_c is the cross section area of the coil, ω_r is the rotor speed, t is time, and phase (φ) is zero for phase A and $\frac{\pi}{2} rad$ for phase B.

Coils are considered to be made by bulk material (one single turn). For multiple turn coils, equation (2) shall be modified to include the number of turns. However, resistive power losses in the winding will remain unchanged.

Total power losses (P_t) in the motor are calculated using (3).

$$P_t = P_w + P_c \qquad (3)$$

Where P_w are the windings resistive losses, and P_c are the core losses in the motor.

Resistive power losses per phase are calculated as:

$$P_{w\_phase} = \left(\frac{J \cdot A_c}{\sqrt{2}}\right)^2 \cdot \rho \frac{l}{A_c} \qquad (4)$$

Where l is the total length of a single phase winding, which is considered to be 4 times the total length of the motor, and ρ is the resistivity of copper that can be calculated, at each temperature (T) as:

$$\rho = \rho_{20} \cdot \left(1 + 3.93 \cdot 10^{-3} \cdot (T - 20)\right) \qquad (5)$$

For the two phases of the motor, total resistive power losses can be simplified to:

$$P_w = J^2 \cdot \rho \cdot l \cdot A_c \qquad\qquad (6)$$

Specific core losses, W/m^3, are, at the same time, calculated using Steinmetz Equation [39]:

$$P_c = K_h f B_m^2 + K_c (f B_m)^2 + K_e (f B_m)^{1.5} \qquad\qquad (7)$$

Steinmetz coefficients for Vacoflux 48 FeCo alloy are obtained from manufacturer core loss curves at frequencies from 0 to 1000 Hz for a lamination thickness of 0.35 mm. Table 3 show the values of such coefficients considered in the model.

Table 3 Steinmetz coefficients for the FeCo alloy.

Coefficient	Value
Hysteresis coefficient, k_h	96.78
Eddy currents coefficient, k_c	0.459
Excess losses coefficient, k_e	0.977

Power losses in the permanent magnet are limited to eddy current losses and core losses of the rotor shaft are neglected. Eddy current dissipation in the coils can be neglected too.

The effects of different geometric and excitation parameters have been analyzed for different sizes to determine torque, motor constants, efficiency and other useful variables as shown in results section.

4   Thermal analytical model for heat dissipation inside human body environments

There is a direct relationship between current density levels in the motor and torque. The higher is the current density, the higher is the torque until saturation of the ferromagnetic yoke. Once ferromagnetic yokes are fully saturated, current density increase still increase total torque but in a lower proportion. However, current density is also linked with the heat generation in the motor as resistive losses depends quadratically on current density. In addition, any increase in temperature means and increase in resistivity which turns out in even higher resistive losses. Therefore, current density in the windings must be limited to prevent overheating and must be analyzed in order to evaluate realistically the behaviour of an electromagnetic motor. Excessive heat in the motor potentially generates a permanent damage in the motor itself and/or in the surrounding environment [40]. This is even more critical for internal medical devices as maximum temperature of the outer surface of the motor shall never be larger than 43 °C, threshold to prevent tissues damages [41].

Size of the motor also directly affects to thermal behaviour and maximum temperature. The heat generated inside the motor can

only be dissipated through the external surface. Ratio between external surface and total volume is a critical factor that determines dissipating capacity of the system. The larger is the external surface with respect to the total volume, the better the dissipation and therefore, the lower the surface temperature for the same volumetric power. This ratio increases with reduction of the size, therefore miniaturized devices can admit much larger volumetric power generation, as shown in equation (6), than larger devices.

This study is oriented for in-body applications; thus three in-body representative scenarios are proposed for the thermal study. In the three proposed scenarios, heat transfer is considered stationary and the motor is defined as perfect cylinder of diameter D and length L placed horizontally in the fluid field. Heat generation inside the motor is considered homogeneous, and the motor surface is considered isothermal. Scenarios I, II and III have been selected focusing on potential operation of the motor inside the human body:

- Scenario I. Respiratory tract: Operation inside the respiratory tract of a micromotor is considered. From the thermal point of view, it is considered that heat is evacuated to static air at ambient pressure and 36ºC. Surface temperature of the motor is limited to 60ºC in order to operate safely, without risk of demagnetization of the magnets and minimizing potential burns to tissues if manipulated by a person. Nevertheless, in this case, it is necessary to avoid any contact with any surrounding tissue. This air environment also serves as reference environment for other types of more common operational scenarios besides specific internal medical applications.

- Scenario II. Body Fluid: Operation of the motor inside human body fluid is considered. Heat is evacuated by natural convection of the motor immersed in the body fluid, with equivalent thermal properties to water at 36ºC [42]. In this case, surface temperature of the motor is limited to 43ºC.

- Scenario III. Blood Torrent: Operation of the motor inside a human aorta is considered. Since the average volumetric blood flow for a male adult is 4.9 l/min [43], and the average size of the aorta artery for a male adult is 25 mm [44], an average blood speed of 0.16 m/s can be defined inside of the aorta. Therefore, heat is evacuated by forced convection to the blood, with equivalent thermal properties to water at 36ºC. Surface temperature of the motor is limited to 43ºC.

Under steady state conditions, heat generated by the motor (P_t) shall be fully dissipated to the environment by convection. This heat is quantified according to the Newton's law of cooling:

$$P_t = h \cdot A_h \cdot (T_s - T_\infty) \qquad (9)$$

Where, h is the average convective heat transfer coefficient,

A_h is the equivalent external area of heat exchange of the motor, T_s is the surface temperature of the motor, and T_∞ is the temperature of the environment.

The convective heat transfer coefficient, h, will change from one scenario to another, since it depends on the geometry of the system and the environmental properties. Convective heat transfer coefficient can be analytically obtained using the formulation of the Nusselt dimensionless number (Nu_L):

$$Nu_L = \frac{h \cdot L}{k_f} \qquad (10)$$

Where, k_f is the heat conduction of the fluid, and L is the characteristic length of the motor.

Then, the maximum current density limit (J_{max}) in each scenario can be defined by combining, (6), (9) and (10) equations as:

$$J_{max} = \left(\frac{Nu_L \cdot k_f}{\rho} \cdot \frac{A_h}{A_c} \cdot (T_s - T_\infty) \right)^{1/2} \qquad (11)$$

For scenario I and II, Nusselt number is calculated based in Churchill and Chu correlation for a horizontal cylinder in natural convection [45]:

$$Nu_L = \left\{ 0.60 + \frac{0.387 Ra_L^{1/6}}{[1 + (0.559/Pr)^{9/16}]^{8/27}} \right\}^2 \qquad (12)$$

Where, Ra is the Rayleigh dimensional number, and Pr is Prandtl dimensionless number.

This equation is valid for all motor scales studied in this paper since $Ra_L < 10^{12}$ in all cases. All properties are evaluated for fluid at film temperature (T_f) :

$$T_f = \frac{T_s + T_\infty}{2} \qquad (13)$$

For scenario III, Nusselt number is calculated using the Zukauskas correlation for a horizontal cylinder in a cross flow [46] :

$$Nu_L = C Re_L^m Pr^n \left(\frac{Pr}{Pr_s} \right)^{\frac{1}{4}}$$

<center>(14)</center>

Where, R_{e_L} is the Reynolds dimensionless number and C, m and n are empirical coefficients that depend on the Reynolds and

Prandtl numbers.

All properties must be evaluated at T_∞ except from Pr that shall be evaluated at T_s. All fluids properties are obtained from

handbook [42].

By using this modelling, relationship between current densities and temperatures of the motor can be analyzed for different

miniaturization values.

5   Results And Discussion

Electromagnetic and thermal models have been used to deeper understand the mechanical and thermal response of the electric

motor for different scales. Results are presented and discussed in this section. Current density is used as main linking parameter as

it affects to cogging torque, thus total torque, efficiency and it also links with the corresponding thermal effects. Electromagnetic

resultas have been obtained by performin multiple 2D transient and parametric simulations.

A. Motor torque, motor constant and torque density

Fig. 3 plots motor torque versus angular position, for a motor with a diameter of 10 mm rotating at 3000 rpm and two current

density values. This level of speed has been chosen to determine a speed that could be achievable by any analyzed size of motors.
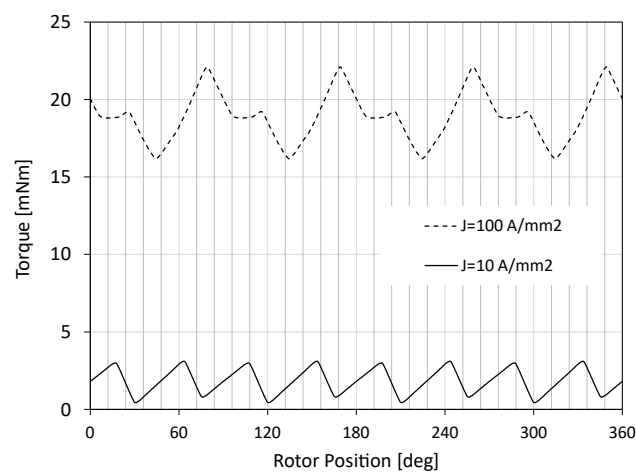

Fig. 3. Torque vs. a full rotation angle for 10 A/mm^2 and 100 A/mm^2 for a 10 mm diameter motor.

It can be observed that the motor output torque is not perfectly constant, but it has variations in respect to a certain average value.

This is caused by the variable reluctance of the airgap that the ferromagnetic core coils generate. This variation is defined as

cogging, or ripple torque. The cogging torque present on the motor performance is a complex discussion (out of the scope of this paper) and depends, among other things, on the specific dimensions of the magnetic elements inside the motor. Motor cogging torque can be simply simulated by performing a parametric rotation simulation of the torque of the rotor with no excitation in the coils.

To properly assess the motor capacity to produce an output useful torque, the average output torque ($|T_m|$) is considered in most of the calculation in this paper:

$$T_m = \frac{T_{max} + T_{min}}{2} \qquad (15)$$

Where, T_{max} is the maximum amplitude of the motor torque in a full electric period, and T_{min} is the minimum amplitude of the output torque in a full electric period.

Cogging torque is the self-locking stall torque, which shall be overcome by circulating currents around the yokes to generate a motion. If circulating currents, and corresponding induction effects on the ferromagnetic yokes, can not overcome this cogging torque, the motor will not be able to move. This lock can always be overcome by injecting larger currents, but, as stated, this increases temperature levels. Besides any thermal limits, there is an electrical effect link where cogging torque is much larger than average motor torque. Cogging torque is frequently considered as a detrimental feature of an electromagnetic motor since it produces a negative impact on the motor performance [47].

Figure 4 shows the average motor torque vs. its characteristic length for various levels of current density in each winding phase. Cogging torque maximum amplitude when no excitation in the coils (J=0 A/mm^2) is also depicted.
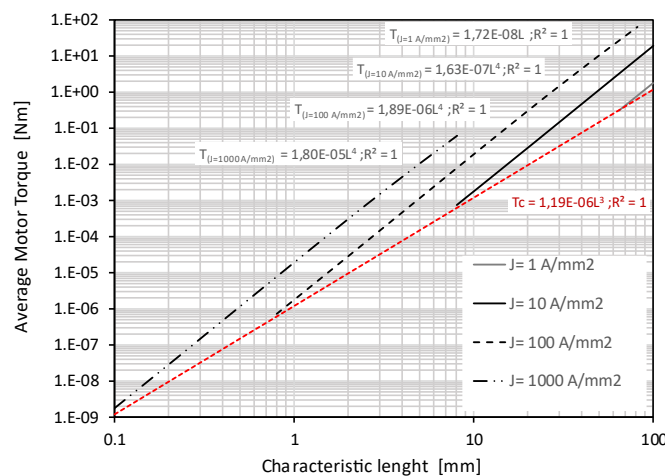

Fig. 4. Average output torque (black lines) and cogging torque (red line) vs. characteristic length.

Results of Fig.4 have been following two main assumptions. First, only those motor sizes that provide a positive value of the

minimum torque in a full electric period are considered. Second, only those values of current density that generates an airgap magnetic flux lower than 1.6 T have been included. This threshold value has been defined to avoid risk of permanent demagnetization of the rotor permanent magnet and magnetic saturation of the ferromagnetic yoke. For current densities below 10 A/mm^2 the airgap magnetic flux density can be considered almost independent of the motor characteristic length and about 0.8±0.03 T.

In Fig.4, it can be observed that the cogging torque of the motor decreases proportional to the volume of the motor (α=3±0.01). However, the average torque produced by the motor is proportional to the fourth exponent (α=4±0.03) independently of the current density in the coils. Therefore, for a specific motor configuration and operational conditions, there is a minimum size where the cogging becomes larger than the produced torque of the motor. Then, cogging torque in the micro-scale limits a practical application of the motor and would ultimately prevent motion of the rotor itself.

From a simple electromechanical point of view with no thermal considerations, the minimum requirements for current density at different sizes are summarized next: 1 A/mm^2 is enough to overcome cogging torque for motors lager than 70 mm diameter. Current density of 10 A/mm^2 is enough to activate motors larger than 8 mm diameter. Current density of 100 A/mm^2 is enough to activate motors larger than 0.8 mm diameter. And current density of 1000 A/mm^2 is enough to activate motors larger than 0.1 mm diameter.

However, these limits are for operation situations where cogging torque have the same value than averages output torque, and therefore, there will be angles where real effective torque will be null and thus, the motor could be stuck at this angle, cogging torque ratio of 100%. A better assessment of the impact of the cogging torque in the motor total output torque can be done by using the cogging torque ratio which is defined as:

$$R_{cogging} = \frac{T_c}{T_m} \tag{16}$$

Where T_m is the magnitude of the average torque in a electric period produced by the motor for a given current density and T_c is the cogging torque evaluated at J=0 A/mm^2.

Results of the cogging ratio vs. characteristic length of the motor at various current density values are plotted in Fig. 5. It can be observed that cogging ratio is inversely proportional to the characteristic length and directly proportional to the current density.
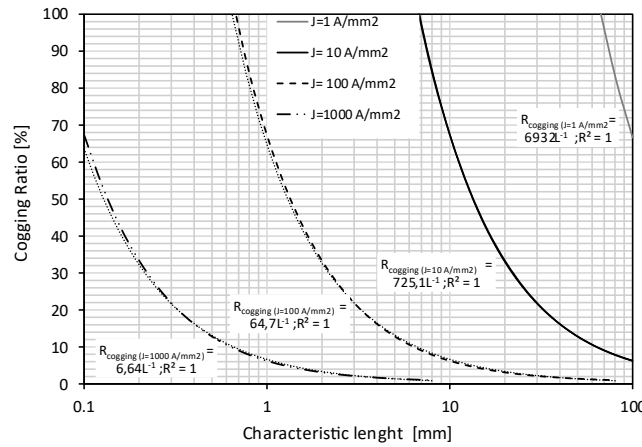
Fig. 5. Cogging ratio vs. characteristic length for 1 to 1000 A/mm^2.

A threshold characteristic length can be defined for different values of cogging ratios and current densities. A cogging ratio of 10% means that the lowest limit of the output effective torque is 10% lower than the average one. Table 4 summarizes the maximum size of the motors for two different cogging ratios of 10% and 50% and various current in the windings.

Table 4 Size of Motor and Current Density Values

Current density, J [A/mm^2]	Maximum size of the motor (Characteristic length) [mm]	
	$R_{cogging} = 10\%$	$R_{cogging} = 50\%$
10	64	12
100	6.4	1.2
1000	0.64	0.12

From Table 4, it can be deduced that it is necessary high current densities to activate miniaturized 2 phase BLDC micromotors, smaller than 2 mm diameter. Such high current densities levels, ranging from 100 to 1000 A/mm^2 are not common values in drivers and wires so special considerations shall be considered when designing control circuits and connections. Such high current density levels will also require extensive and specific thermal analysis to prevent damages of the wires and connections, as described in sub-section B of this section.

Motor constant is calculated for different sizes and current densities and describes using Eq. 17. The motor constant depends quadratically on the characteristic length and it is independent on the current density in the windings within the explored range in this paper.

$$K_T \approx 1.01 \cdot L^2 \tag{17}$$

This can be explained considering that the motor constant depends upon the configuration of the motor and the total current in the windings is proportional to the square of the characteristic length of the motor.

Finally, the torque density (ρ_{T_m}) of the active magnetic part of the motor is obtained (see Fig. 6) assuming the motor volume as that of a cylinder. Since D=L:

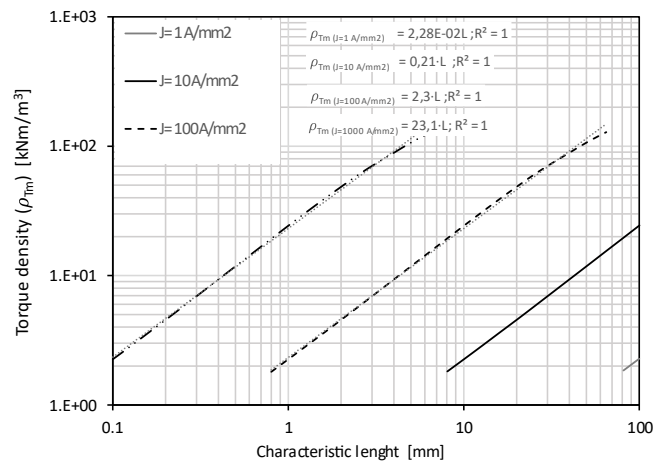$$\rho_{Tm} = \frac{4 \cdot T_u}{\pi \cdot L^3} \qquad\qquad (18)$$

Fig. 6. Torque density vs. characteristic length for J=1 to 1000 A/mm^2.

Torque density depends linearly on the characteristic length of the motor and therefore on the scale factor (α=1±0.05). Torque density, is linearly dependent on the current density too.

Note that for motors smaller than 1 mm in size with current densities J=100 and J= 1000 A/m^2, the achieved torque density is, at least, one order of magnitude larger than those of the state of the art (see Table 1). This can be achieved because ferromagnetic yokes are considered, differently than any other previous work in motors smaller than 1 mm.

B. *Power losses, thermal behaviour and efficiency*

Power losses inside an electromagnetic motor generate heat that increase motor temperature. Maximum allowable temperature shall be defined to assure a safe operation of the motor. In order to calculate such temperature increase, power losses are calculated at different motor sizes, rotational speeds and current densities. As an example, Fig. 7**¡Error! No se encuentra el origen de la referencia.** shows the power losses of the motor, including resistive losses, eddy current losses and core magnetic losses, when it rotates at a constant speed of 3000 rpm and for a current density J=10 A/mm2.
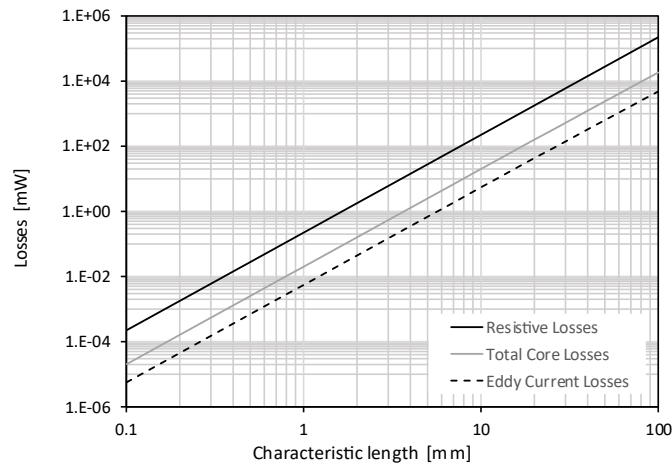
Fig. 7. Power losses vs. characteristic length for 10 A/mm^2 at 3000 rpm.

In Fig. 7, it can be observed that power losses are dominated by the resistive losses, and in second term by core losses. Eddy current losses are neglectable in the windings for all characteristic lengths studied in this paper.

Fig. 8¡**Error! No se encuentra el origen de la referencia.** shows total power losses in the motor according to (*3*) for various values of current density for 3000 rpm.
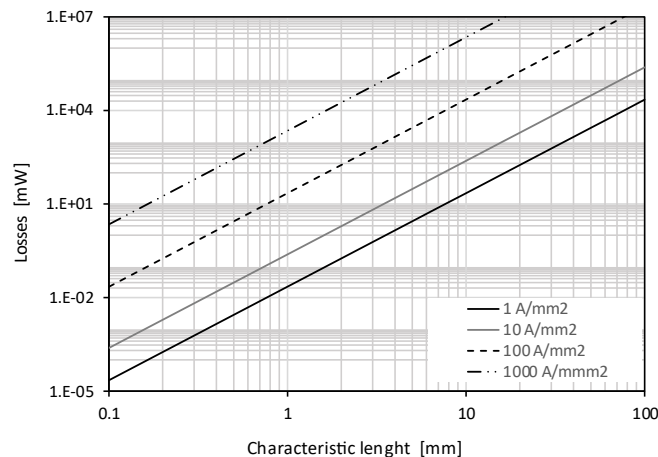

Fig. 8. Total core losses vs. characteristic length for 1 to 1000 A/mm^2 at 3000 rpm.

Heat generation depends on the volume of the motor (α=3). However, the heat evacuation to the environment, according to (9) is proportional to the motor external surface (α=2). Therefore, the lower the scale, the higher the current density that the motor can withstand for a defined maximum operational temperature of the motor. Maximum current density vs. characteristic length of the motor for the three thermal scenarios introduced in section III is plotted in Fig. 9¡**Error! No se encuentra el origen de la referencia.** for an operation at 3000 rpm.
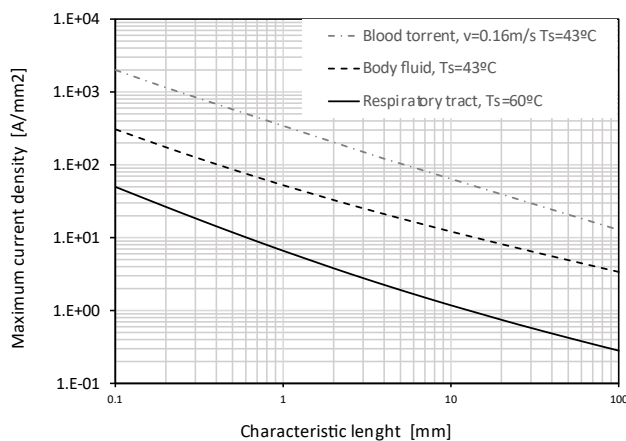
Fig. 9. Current density vs characteristic length for the three different thermal scenarios.

In all scenarios cases, the maximum current density inversely depends on the characteristic length as (approximately):

$$J_{max} \propto L^{-0.7 \pm 0.05} \tag{19}$$

This results are coherent with the dependency of the heat transfer coefficient defined in [32] and described in the introduction. As expected, the boundary conditions of the surrounding environment highly influence the maximum allowable current density in the windings. As an example, Table 5 summarizes the maximum current density admissible for different motor sizes (L) between 0.1 and 10 mm for the three different thermal scenarios.

Table 5 Threshold Length and Current Density Values

Thermal Scenario	Maximum current density, J [A/mm²] for characteristic length		
	0.1 *mm*	1*mm*	10 *mm*
I	50	6	1.2
II	305	55	12
III	1954	335	62

This useful result can be used for a definition of the maximum current limit of ferromagnetic core-coils BLDC motors operating inside the human body in combination with limits given from the cogging torque analysis.

An analysis of the efficiency of the motor has also been done. Efficiency of the motor is calculated as:

$$E_{ff} = \frac{T_m \cdot \omega_r}{T_m \cdot \omega_r + P_t} \qquad (19)$$

Fig. 10 shows the efficiency of the electromagnetic motor vs. characteristic length for various values of current density in the windings when rotor speed is $\omega_r = 3000$ rpm.
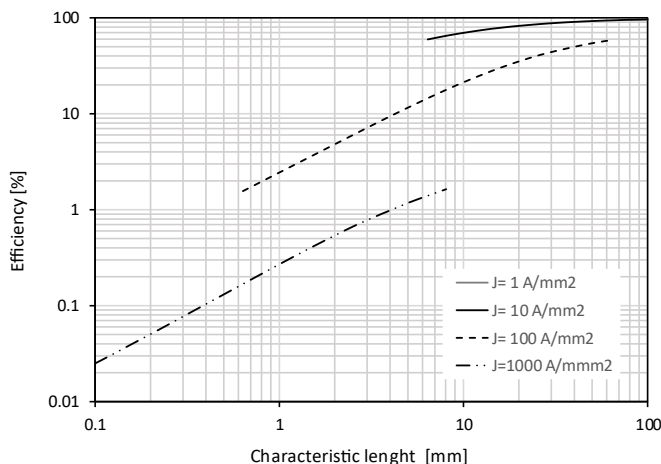

Fig. 10. Efficiency vs. characteristic length for 1 to 1000 A/mm^2.

Efficiency curves do not perfectly match an exponential fit, however, for a characteristic length below 2 mm, efficiency decreases linearly with the scale factor (α). For motors larger than 8 mm size, reasonable efficiencies between 60 to 40% can be achieved. However, it is significant for the miniaturization analysis that efficiencies of motors smaller than 1 mm, are very reduced, being lower than 3 %. This is due to the fact that induction of the ferromagnetic yoke suffers from a sever negative scale down effect. Therefore, in the micro-scale, it is necessary very high current levels to induce and saturate ferromagnetic yokes. It must also be considered that 3000 rpm is very low speed for reduced size motors: ultralow inertia of the rotors would allow much higher speed than for larger motors, and thus larger efficiencies as shown in Fig. 11. In any case, such a low efficiency should not be a real problem if the motor is connected catheter and power from a macroscopic power supply, nevertheless, this can be a big issue for battery or wireless transfer powered implantable devices

Efficiency is directly related with rotational speed. Fig. 11 shows the motor efficiency vs rotor speed at various motor characteristic lengths. The current density values for each motor size have been designed in accordance to the threshold values of Scenario III in Table 5. For micromotors smaller than 1 mm diameter, it is necessary to achieve very high speeds to obtain reasonable levels of efficiency. As shown in Fig. 11, a motor of 1 mm diameter can provide 15% of efficiency operating at 20000 rpm. It is well known that, for smaller motor characteristic lengths the maximum rotor speed can be considerably increased. Discussion on a speed limit vs. motor size is complex and out of the scope of this paper. However, for the shake of comparison, rotor speeds over 100000 rpm have been previously reported for motors of a few mm in diameter with an efficiency of 11% [48,49].
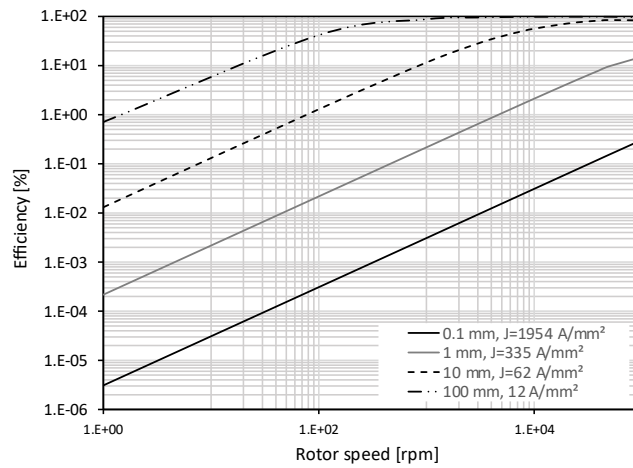
Fig. 11. Motor efficiency vs. rotor speed for various motor characteristic lengths and maximum current densities in thermal scenario III.

Scalability laws can be useful for designing purposes towards miniaturized motors. Table 6 summarizes the exponential factor (α) of the different scale dependent functions that define the main performance of the motor.

Table 6 α Values for the Motor Configuration Variables

Parameter	Value of α
Motor torque	4
Motor torque density	1
Cogging torque	3
Maximum current density	-0.7
Efficiency (L<2 mm)	≈1

C. Applications cases

Estimation of the performance of the motors requires the combination of all the design guide rules given in previous sub-sections. The information of output torque, Fig. 4, and cogging torque ratio, Fig. 5. for different current densities must be merged with the information about the limits imposed by thermal issues, Fig. 9. Table 7 depicts maximum average output torque and cogging torque ratio for different motor size and thermal scenarios.

Table 7 Expected torque and cogging torque ratio of micromotors in different thermal scenarios

Thermal Scenario	Micromotor size		
	0.1 mm	1 mm	10 mm
I	$1 \cdot 10^{-9}$ Nm 100%	$1 \cdot 10^{-6}$ Nm 96%	$1 \cdot 10^{-3}$ Nm 85%
II	$3 \cdot 10^{-9}$ Nm 85%	$1.7 \cdot 10^{-6}$ Nm 70%	$2 \cdot 10^{-3}$ Nm 50%
III	$1 \cdot 10^{-8}$ Nm 20%	$5 \cdot 10^{-6}$ Nm 18%	$6 \cdot 10^{-3}$ Nm 15%

Table 7 represents specific examples of miniaturized motors suitable for internal medical devices and their expected performance. Low cogging torque values are achieved for all motor sizes in thermal scenario III as heat dissipation is large enough to withstand

very high current density. In thermal scenario II, medium values of cogging ratio are found, but they are large enough to provide a certain effective output torque, at any size. This demonstrates an adequate thermo-electrical behavior of the proposed design for miniaturized internal medical applications.

On the other hand, first thermal scenario, where dissipation capacity is much more reduced, does not permit to operate micrometric size motors like the designed one since current density are very limited. The maximum applicable motor size has been found in around 4 mm. To improve this pitfall of scenario I, the maximum allowable temperature on surface, which for this study has been conservatively set in 60 ºC, could be larger if wire coating materials allows larger operational temperature. It is remarkable that the smallest BLDC ferromagnetic yoke motors commercially available are between 5 to 8 mm diameter, reaffirming the results of our analysis. An alternative to avoid cogging torque issues is to use flux modulators pole pieces, like Vernier or magnetic gears include, at the expense of a more complex construction model.

With table 7 values, different new medical tools applications could be depicted. For example, a multiaxis steerable catheter including a set of 1 mm diameter high torque micromotors could be developed to allow motion of the catheter through intricate vessels paths. Another example is multiaxis microrobotic tweezers that could use ultrasmall 0.1 mm motors to be activated and in this way, surgery and arthroscopies tools would require smaller patient access.

6   Conclusion

We have theoretically studied which are the operational limits and the expected performance inside different human body environment as long as the motor is miniaturized. This permits to determine the maximum expected performance and torque values for different sizes of micromotors.

A thermo-electrical analysis of scale effects of a 2-phase permanent magnet BLDC motor for internal medical devices of a has been completed for motor sizes between 0.1 to 100 mm. The electromagnetic behaviour of the motor has been analysed by using a parametric 2D transient finite element model. In addition, a thermal analytical model for heat dissipation inside human body environments. Heading towards the applications of micromotors for biomedical applications, three scenarios have been explored: operation in the blood torrent, body fluid and respiratory tract.

The effects of different geometric and excitation parameters have been analyzed for sizes from 0.1 to 100 mm to calculate torque, cogging torque, motor constant, torque density and efficiency.

Cogging torque in the micro-scale severely limits a practical application of motor and would ultimately prevent motion of the rotor itself. From a simple electromechanical point of view with no thermal considerations, the minimum requirements for current density at different sizes are summarized next: 1 A/mm^2 is enough to overcome cogging torque for motors lager than 70 mm

diameter. Current density of 10 A/mm^2 is enough to activate motors larger than 8 mm diameter. Current density of 100 A/mm^2 is enough to activate motors larger than 0.8 mm diameter. And current density of 1000 A/mm^2 is enough to activate motors larger than 0.1 mm diameter. It is necessary high current densities to activate miniaturized 2 phase BLDC micromotors, smaller than 2 mm diameter. Such high current densities levels, ranging from 100 to 1000 A/mm^2 are not common values in drivers and wires so special considerations shall be considered when designing control circuits.

Estimation of the performance of the motors requires the combination of all the design guide rules: output torque, cogging torque ratio must be merged with the information about the limits imposed by thermal issues.

Low cogging torque values are achieved for all motor sizes in thermal scenario III. In thermal scenario II, medium values of cogging ratio are found, but they are large enough to provide a certain effective output torque, at any size. This demonstrates an adequate thermo-electrical behavior of the proposed design for miniaturized internal medical applications.

On the other hand, first thermal scenario, does not permit to operate micro-metric size motors like the designed one since current density are very limited. The maximum applicable motor size has been found in around 4 mm.

Results demonstrate the potential operation of high torque density micromotors with ferromagnetic core coils, in diameters between 0.1 and 1 mm, requires current densities between 100 and 1000 A/mm2. This can be admissible in internal medical applications where heat dissipation capacity is very large. Miniaturization of this type of motors can mean the future development of micro-robotic arms, steerable smart catheters or minimally arthroscopies tools actuated by one or several high torque micromotors. This reinforces the interest of going deeper in the development of miniaturized high torque motors, analyzing other aspects like bearings resistive torques, full electromechanical 3D design, manufacturability and assembly, and of course, demonstration through testing. Specific examples and expected performance for different sizes of motors are given in final section.

This work has to be seen as a design route map to know what performance level can be expected for different sizes of micromotors. This work can save many time in determining those limits to any other researcher working in micromotors because the information given permit to start any design from a forward design position, instead of starting from scratch.

Funding Data

References

[1]   Baltzer, M., and Obermeier, E., 1997, "A Micro Shutter for Applications in Optical and Thermal Detectors," pp. 67–70.

[2]   Mourlas, N. J., Stark, K. C., Mehregany, M., and Phillips, S. M., 1996, "Exploring Polysilicon Micromotors for Data Storage Micro Disks," Proc. IEEE Micro Electro Mech. Syst., pp. 198–203.

[3]   Bodnicki, M., Wierciak, J., Credo, W., Bagiński, K., and Wawrzyniuk, L., 2018, "Electromagnetic Angular Positioner Based on DC Micromotor," MATEC Web Conf., **157**.

[4]   Suzumori, K., Miyagawa, T., Kimura, M., and Hasegawa, Y., 1999, "Micro Inspection Robot for 1-in Pipes," IEEE/ASME Trans. Mechatronics, **4**(3), pp. 286–292.

[5]   Thielicke, E., and Obermeier, E., 2000, "Microactuators and Their Technologies," Mechatronics, **10**(4), pp. 431–455.

[6]   Shumbayawonda, E., Salifu, A. A., Lekakou, C., and Cosmas, J. P., 2018, "Numerical and Experimental Simulations of the Wireless Energy Transmission and Harvesting by a Camera Pill," J. Med. Devices, Trans. ASME, **12**(2).

[7]   Sheerer, C. D., Drozek, D., and Choi, J., 2015, "A Hand-Held Device for Controlling a Mounted, Motor Driven Colonoscope," J. Med. Devices, Trans. ASME, **9**(3).

[8]   Peng, J., Ma, L., Li, X., Tang, H., Li, Y., and Chen, S., 2019, "A Novel Synchronous Micro Motor for Intravascular Ultrasound Imaging," IEEE Trans. Biomed. Eng., **66**(3), pp. 802–809.

[9]   Kode, V. R. C., and Çavuşoğlu, M. C., 2007, "Design and Characterization of a Novel Hybrid Actuator Using Shape Memory Alloy and DC Micromotor for Minimally Invasive Surgery Applications," IEEE/ASME Trans. Mechatronics, **12**(4), pp. 455–464.

[10]   Munoz, F., Alici, G., and Li, W., 2016, "A Magnetically Actuated Drug Delivery System for Robotic Endoscopic Capsules," J. Med. Devices, Trans. ASME, **10**(1).

[11]   Wang, T., Lancée, C., Beurskens, R., Meijer, J., Knapen, B., Van Der Steen, A. F. W., and Van Soest, G., 2014, "Development of a High-Speed Synchronous Micro Motor and Its Application in Intravascular Imaging," Sensors Actuators, A Phys., **218**, pp. 60–68.

[12]   Su, H., Hu, Y., Karimi, H. R., Knoll, A., Ferrigno, G., and De Momi, E., 2020, "Improved Recurrent Neural Network-Based Manipulator Control with Remote Center of Motion Constraints: Experimental Results," Neural Networks, **131**, pp. 291–299.

[13]   Su, H., Qi, W., Hu, Y., Karimi, H. R., Ferrigno, G., and Momi, E. De, 2022, "An Incremental Learning Framework for Human-Like Redundancy Optimization of Anthropomorphic Manipulators," IEEE Trans. Ind. Informatics, **18**(3), pp. 1864–1872.

[14]   Perez-Diaz, J. L., Diez-Jimenez, E., Valiente-Blanco, I., Cristache, C., Alvarez-Valenzuela, M.-A., and Sanchez-Garcia-Casarrubios, J., 2014, "Contactless Mechanical Components: Gears, Torque Limiters and Bearings," Machines, **2**(4).

[15]   Perez-Diaz, J. L., Diez-Jimenez, E., Valiente-Blanco, I., Cristache, C., Alvarez-Valenzuela, M.-A., Sanchez-Garcia-Casarrubios, J., Ferdeghini, C., Canepa, F., Hornig, W., Carbone, G., Plechacek, J., Amorim, A., Frederico, T., Gordo, P., Abreu, J., Sanz, V., Ruiz-Navas, E.-M., and Martinez-Rojas, J.-A., 2015, "Performance of Magnetic-Superconductor Non-Contact Harmonic Drive for Cryogenic Space Applications," Machines, **3**(3).

[16]   Diez-Jimenez, E., Sanchez-Montero, R., and Martinez-Muñoz, M., 2017, "Towards Miniaturization of Magnetic Gears: Torque Performance Assessment," Micromachines, **9**(1).

[17]   Perez-Diaz, J. L., Valiente-Blanco, I., Cristache, C., Sanchez-García-Casarubios, J., Rodriguez, F., Esnoz, J., and Diez-Jimenez, E., 2019, "A Novel High Temperature Eddy Current Damper with Enhanced Performance by Means of Impedance Matching," Smart Mater. Struct., **28**(2).

[18]   2021, "ULTRA-EFFICIENT WIRELESS POWERED MICRO-ROBOTIC JOINT FOR HEALTH APPLICATIONS" [Online]. Available: www.uwipom2.eu. [Accessed: 25-Oct-2021].

[19]   J.Esnoz-Larraya;, I.Valiente-Blanco;, C.Cristache;, J.Sanchez;, F.Rodriguez-Celis;, E.Diez-Jimenez;, and J.L.Perez-Diaz, 2017, "OPTIMAGDRIVE: High Performance Magntic Gears Development for Space Applications," *17th European Space Mechanisms and Tribology Symposium*, Hatfield, UK, pp. 1–5.

[20]   Koser, H., and Lang, J. H., 2006, "Magnetic Induction Micromachine—Part II: Fabrication and Testing Florent," J. Microelectromechanical Syst., **15**(2), pp. 415–426.

[21]   Arnold, D. P., Das, S., Cros, F., Zana, I., Allen, M. G., Member, S., and Lang, J. H., 2006, "Magnetic Induction Machines Integrated Into Bulk-Micromachined Silicon," J. micromechanical Syst., **15**(2), pp. 406–414.

[22]   Dario, P., Carrozza, M. C., Stefanini, C., and D'Attanasio, S., 1998, "A Mobile Microrobot Actuated by a New Electromagnetic Wobble Micromotor," IEEE/ASME Trans. Mechatronics, **3**(1), pp. 9–16.

[23]   Kim, J. H., Jung, I. S., and Sung, H. G., 2006, "Design and Manufacturing of Ultra Small Actuator," *2006 IEEE International Conference on Mechatronics, ICM*, pp. 23–26.

[24]   Merzaghi, S., Koechli, C., and Perriard, Y., 2011, "Development of a Hybrid MEMS BLDC Micromotor," IEEE Trans. Ind. Appl., **47**(1), pp. 3–11.

[25]   Williams, C. B., Shearwood, C., Mellor, P. H., and Yates, R. B., 1997, "Modelling and Testing of a Frictionless Levitated Micromotor," Sensors Actuators, A Phys., **61**(1–3), pp. 469–473.

[26]   Lyshevski, S. E., Nazarov, A., and Boggs, J., 2002, "Integrated Micro- and Miniscale Electromechanical Systems with Permanent-Magnet Servo-Motors and VLSI Drivers-Controllers," Mechatronics, **12**(9–10), pp. 1115–1131.

[27]   Diez-Jimenez, E., Rizzo, R., Gómez-García, M. J., and Corral-Abad, E., 2019, "Review of Passive Electromagnetic

          Devices for Vibration Damping and Isolation," Shock Vib., **2019**.

[28]   Diez-Jimenez, E., Alén-Cordero, C., Alcover-Sánchez, R., and Corral-Abad, E., 2021, "Modelling and Test of an

          Integrated Magnetic Spring-Eddy Current Damper for Space Applications," Actuators, **10**(1), pp. 1–18.

[29]   Han, D., Nagai, K., and Shinshi, T., 2020, "Micro Electromagnetic Flat Motor Using an 80-Poles and 0.3-Mm-Thick

          Ring Magnet for High Torque," Proc. IEEE Int. Conf. Micro Electro Mech. Syst., **2020**-**Janua**, pp. 509–512.

[30]   K. J. Binns D. W. Shimmi, 1995, "The Relationship Between Performance Characteristics and Sizes of Permanent

          Magnet Motors," *Electrical Machines and Drives*, pp. 423–427.

[31]   Liu, D. K. C., Friend, J., and Yeo, L., 2010, "A Brief Review of Actuation at the Micro-Scale Using Electrostatics,

          Electromagnetics and Piezoelectric Ultrasonics," Acoust. Sci. Technol., **31**(2), pp. 115–123.

[32]   Peirs, J., Reynaerts, D., and Van Brussel, H., 1998, "Scale Effects and Thermal Considerations for Micro-Actuators,"

          Proc. - IEEE Int. Conf. Robot. Autom., **2**(May), pp. 1516–1521.

[33]   Narayanan, A. M., and Bertrand, A., 2020, "Analysis of Miniaturization Effects and Channel Selection Strategies for

          EEG Sensor Networks with Application to Auditory Attention Detection," IEEE Trans. Biomed. Eng., **67**(1), pp. 234–

          244.

[34]   Lin, C. L., Srivastava, A., Coffey, D., Keefe, D., Horner, M., Swenson, M., and Erdman, A., 2014, "A System for

          Optimizing Medical Device Development Using Finite Element Analysis Predictions," J. Med. Devices, Trans. ASME,

          8(2).

[35]   Hopf, R., Gessat, M., Russ, C., Sündermann, S. H., Falk, V., and Mazza, E., 2017, "Finite Element Stent Modeling for

          the Postoperative Analysis of Transcatheter Aortic Valve Implantation," J. Med. Devices, Trans. ASME, **11**(2).

[36]   Arnold, D. P., and Wang, N., 2009, "Permanent Magnets for MEMS," J. Microelectromechanical Syst., **18**(6).

[37]   Muñoz-Martínez, M., Diez-Jimenez, E., Gómez-García, M. J., Rizzo, R., and Musolino, A., 2019, "Torque and Bearing

          Reaction Forces Simulation of Micro-Magnetic Gears," Appl. Comput. Electromagn. Soc. J., **34**(4), pp. 541–546.

[38]   Martinez-Muñoz, M., DIez-Jimenez, E., Sanchez-Montero, R., Lopez-Espi, P. L., and Martinez-Rojas, J. A., 2019,

          "Analysis of the Geometric Parameters Influence in PCB Fixtures for 2D Multipole Magnetization Patterning of Thin

          Layer Micro-Magnets," Int. J. Appl. Electromagn. Mech., **61**(1).

[39]   Steinmetz, C. P., 1892, "On the Law of Hysteresis (Part II) and Other Phenomena of the Magnetic Circuit," Trans. Am.

          Inst. Electr. Eng., **9**(1), pp. 619–758.

[40]   Valiente-Blanco, I., Perez-Diaz, J. L., Perez-Del-Alamo, J. L., and Diez-Jimenez, E., 2020, "Temperature Dependence of

          the Friction Coefficient of Grease-Lubricated PTFE Linear Bushings against Titanium Grade 5 Alloy (Ti6Al4V) and

Life Tests Operating at High-Speed," J. Tribol., **142**(9), pp. 1–7.

[41] Yarmolenko, P. S., Moon, E. J., Landon, C., Manzoor, A., Hochman, D. W., Viglianti, B. L., and Dewhirst, M. W., 2011, "Thresholds for Thermal Damage to Normal Tissues: An Update," Int. J. Hyperth., **27**(4), pp. 320–343.

[42] Frank P. Incopera, 2015, *Fundamentals of Heat and Mass Transfer*, John Wilet & Sons.

[43] Betts, G., and Dsaix, P., 2013, "Anatomy & Physiology Vol 2," *Anatomy & Physiology*, OpenStax College, pp. 837–903.

[44] Syed, M. N., Ahmad, M. M., Ahmad, M. N., Hussaini, S., Muhammad, M. N., Pir, S. H. A., Khandheria, B. K., Tajik, A. J., and Ammar, K. A., 2017, "Normal Diameter of the Ascending Aorta in Adults: The Impact of Stricter Criteria on Slection of Subjects Free of Disease," J. Am. Coll. Cardiol., **69**(11 Supplement), p. 2075.

[45] Churchill, S.W. and Chu, H. H. S., 1975, "Correlating Equations for Laminar and Turbulent Free Convection from a Vertical Plate," Int. J. Heat Mass Transf., **18**, pp. 1323, 1329.

[46] Zukauskas, A., 1972, "Heat Transfer from Tubes in Crossflow," Adv. Heat Transf., **8**, pp. 93–160.

[47] Bianchi, N., and Bolognani, S., 2002, "Design Techniques for Reducing the Cogging Torque in Surface-Mounted PM Motors," IEEE Trans. Ind. Appl., **38**(5), pp. 1259–1265.

[48] Gilles, P. A., Delamare, J., Cugat, O., and Schanen, J. L., 2000, "Design of a Permanent Magnet Planar Synchronous Micromotor," Conf. Rec. - IAS Annu. Meet. (IEEE Ind. Appl. Soc., **1**, pp. 223–227.

[49] Achotte, N., Gilles, P. A., Cugat, O., Delamare, J., Gaud, P., and Dieppedale, C., 2006, "Planar Brushless Magnetic Micromotors," J. Microelectromechanical Syst., **15**(4), pp. 1001–1014.

Figure caption list

Fig. 1. Cross-section of the motor.

Fig. 2. Magnetic flux inside 1mm motor.

Fig. 3. Torque vs. a full rotation angle for 10 A/mm2 and 100 A/mm2 for a 10 mm diameter motor.

Fig. 4. Average output torque (black lines) and cogging torque (red line) vs. characteristic length.

Fig. 5. Cogging ratio vs. characteristic length for 1 to 1000 A/mm2.

Fig. 6. Torque density vs. characteristic length for J=1 to 1000 A/mm2.

Fig. 7. Power losses vs. characteristic length for 10 A/mm2 at 3000 rpm.

Fig. 8. Total core losses vs. characteristic length for 1 to 1000 A/mm2 at 3000 rpm.

Fig. 9. Current density vs characteristic length for the three different thermal scenarios.

Fig. 10. Efficiency vs. characteristic length for 1 to 1000 A/mm2.

Fig. 11. Motor efficiency vs. rotor speed for various motor characteristic lengths and maximum current densities in thermal

scenario III.

Table caption list

Table 1 Electromagnetic motor characteristics

Table 2 Values for 1 Milimeter Diameter Motor

Table 3 Steinmetz coefficients for the FeCo alloy.

Table 4 Size of Motor and Current Density Values.

Table 5 Threshold Length and Current Density Values.

Table 6 α Values for the Motor Configuration Variables

Table 7 Expected torque and cogging torque ratio of micromotors in different thermal scenarios